Optics Letters

High-range-resolution and long-distance CO_2 profiling using a single-photon differential absorption lidar

MINGJIA SHANGGUAN,* SIMIN LIN, XIANGHUI GUO, JINXIAN FANG, AND GUOJING DONG

State Key Laboratory of Marine Environmental Science, College of Ocean and Earth Sciences, Xiamen University, Xiamen 361102, China
**mingjia@xmu.edu.cn*

Received 23 November 2025; revised 9 December 2025; accepted 9 December 2025; posted 10 December 2025; published 21 December 2025

Lidar has become an increasingly attractive approach for CO_2 monitoring. However, simultaneously achieving long-range detection and high-range resolution remains a fundamental tradeoff. To address this issue, first, a superconducting nanowire single-photon detector is integrated into lidar to significantly enhance long-range sensitivity, enabling detection of backscattered signals up to 10 km. In addition, a new retrieval algorithm is proposed to retrieve range-resolved CO_2 concentrations from high-SNR column measurements, effectively improving profile resolution and stability. Three consecutive nights of field tests show that the system achieves 30 m range resolution, 5 min temporal resolution, and a near-8-km range. Compared with the traditional CO_2 retrieval algorithm, the proposed method improves the range resolution by more than one order of magnitude while still achieving a 3.8-fold enhancement in retrieval accuracy. Cross-validation with *in-situ* observations shows that the standard deviation between the two datasets is approximately 10 ppm, further confirming the accuracy and robustness of the method. This work underpins future high-resolution CO_2 monitoring networks and supports carbon-cycle studies.

https://doi.org/10.1364/OL.585665

Carbon dioxide (CO_2) is the most significant anthropogenic greenhouse gas, and its accurate observation is essential for understanding carbon-cycle processes, evaluating emission reduction strategies, and improving climate prediction models [1]. In particular, high-spatiotemporal-resolution profiling of CO_2 in the lower troposphere is crucial for revealing boundary-layer dynamics, quantifying surface–atmosphere fluxes, and constraining atmospheric transport in inversion frameworks [2].

Lidar—offering strong atmospheric penetration, high measurement precision, and continuous day-and-night operation—has become a highly attractive approach for CO_2 monitoring. It is generally implemented as either integrated-path or range-resolved differential absorption lidar (DIAL). Integrated-path differential absorption lidar (IPDL)—including dual-wavelength [3] and multi-wavelength approaches [4]—typically sacrifices range resolution to achieve high precision and high temporal resolution, and is widely deployed on spaceborne [5,6] and airborne platforms [7]. In contrast, range-resolved differential absorption lidar (RRDL) provides range-resolved CO_2 profiles but typically sacrifices temporal resolution and retrieval accuracy.

Tremendous efforts have been devoted to advancing RRDL for long-distance CO_2 profiling with high-range resolution. To extend the detection range, existing systems are typically optimized from both the transmitter and receiver sides—either by increasing the single-pulse energy or by enhancing the detection sensitivity. For example, 2-μm amplified nested-cavity OPOs have been developed, delivering ~8 mJ pulse energy [8]. On the receiver side, both direct-detection schemes using superconducting nanowire single-photon detectors (SNSPD) [9] and coherent-detection with local-oscillator amplification [10] have been proposed. However, current RRDL have yet to surpass a detection range of 6 km.

Moreover, improving high-range resolution is likewise a major technical challenge for RRDL. To extend the detection range, RRDL systems commonly select CO_2 absorption lines with moderate absorption coefficients—such as those near 1.57 μm or 2.005 μm—to avoid excessive attenuation during atmospheric transmission [11]. However, weaker absorption inevitably reduces the differential signal between on-line and off-line signals, making it necessary to relax the range resolution to maintain adequate retrieval accuracy. In fact, the highest reported range resolution for RRDL systems is still limited to approximately 120 m [10]. Therefore, simultaneously attaining high-range resolution and long detection range is a fundamental challenge for RRDL.

To address this challenge, a single-photon CO_2 lidar system incorporating a new retrieval algorithm is proposed and demonstrated. The lidar system enhances detection sensitivity by employing an eight-pixel cascaded SNSPD array. Owing to its high count rate, high quantum efficiency, low dark count rate, and absence of afterpulsing, the system acquires high signal-to-noise-ratio (SNR) lidar backscattered signals and achieves a substantially extended detection range [12]. Furthermore, an innovative retrieval framework is developed to derive high-range-resolution CO_2 profiles from path-integrated CO_2 profiles. With this combined hardware–algorithm design, the system achieves

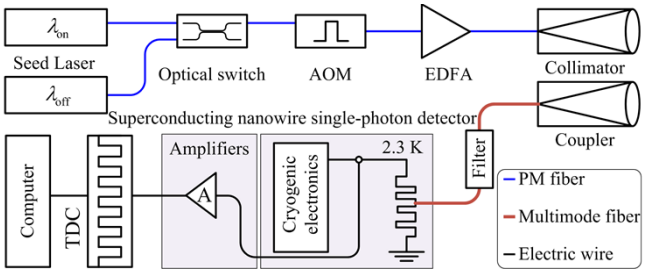

Fig. 1. Optical layout of the lidar. AOM, acoustic-optic modulator; EDFA, erbium doped fiber amplifier; PM fiber, polarization maintaining fiber; TDC, time-to-digital converter.

an effective detection range of nearly 8 km at a range resolution of 30 m and a temporal resolution of 5 min.

The schematic of the single-photon CO_2 lidar system is shown in Fig. 1. The system uses a classical DIAL setup in which two continuous-wave (CW) frequency-stabilized seed lasers at 1572.335 and 1572.45 nm provide the on- and off-line wavelengths, each featuring a 2 MHz linewidth and <5 MHz/day frequency stability. The two CW lasers are alternately switched by an optical switch with a 100 ns rise time and subsequently shaped into ~100 ns pulses by an acousto-optic modulator (AOM) driven at 80 MHz. After amplification by an erbium doped fiber amplifier (EDFA), 32 μJ pulses are produced at a 10 kHz repetition rate. The transmitted beam is collimated using a fiber collimator with an 80 mm focal length and a 12.8 mm effective aperture. The backscattered signal is collected by an identical collimator and coupled into a multimode fiber (62.5 μm core, NA = 0.22). A 0.5 nm bandwidth fiber filter suppresses background noise before the signal enters the detector. The detector is the SNSPD with ~40% efficiency at 1572 nm, <100 cps dark count rate, a 100 Mcps saturation rate, and no afterpulsing. Its output is recorded by a time-to-digital converter (TDC) with a timing precision of 50 ps, and the CO_2 profile is finally retrieved on a computer.

The workflow for retrieving the CO_2 concentration (X_{CO_2}) profile from lidar backscattered signals is illustrated in Fig. 2. The lidar equation can be expressed as:

$$P_i(x_i, R) = P_0 \cdot O(R) \cdot K \cdot A_t \cdot \beta(x_i, R) \cdot T_r^2(x_i, R)/R^2, \quad (1)$$

where P_i is the received photon count, P_0 is the transmitted photon count, x_i is the laser frequency, with x_{on} tuned to the CO_2 absorption line and x_{off} placed in a nearby spectral region where CO_2 absorption is negligible. R is the range, and K is a system constant that includes the optical efficiency of the transmitter/receiver and the detector quantum efficiency. A_t is the telescope aperture area, $O(R)$ is the geometric overlap factor, and β represents the Mie 180° volume backscatter coefficient. And T_r is the atmospheric transmission term, which is expressed as:

$$T_r(x_i, R) = \exp\left\{-\int_0^R [\alpha_a(x_i, R) + \alpha_s(x_i, R)]\, dr\right\}, \quad (2)$$

where α_a is the aerosol extinction coefficient, and $\alpha_s = \alpha + \alpha_m$ is the molecular extinction coefficient composed of the CO_2 absorption coefficient α and the extinction α_m from other atmospheric species.

As shown in Fig. 2, the signals P_{on} and P_{off} are processed by background noise removal, followed by correction for count-rate nonlinearity (deviation of recorded counts at high flux) and

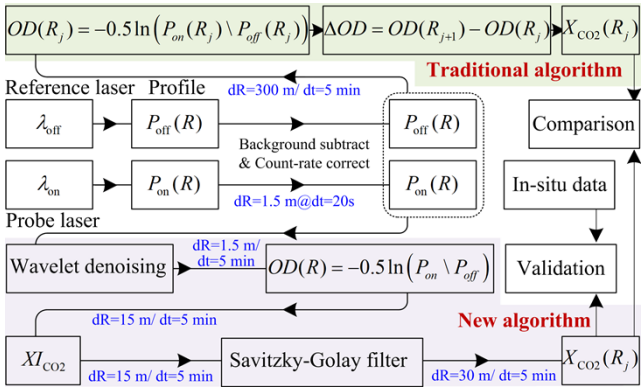

Fig. 2. Workflow for X_{CO_2} profile retrieval using the traditional and the proposed algorithms, with the distance resolution (dR) and temporal resolution (dt) highlighted in blue.

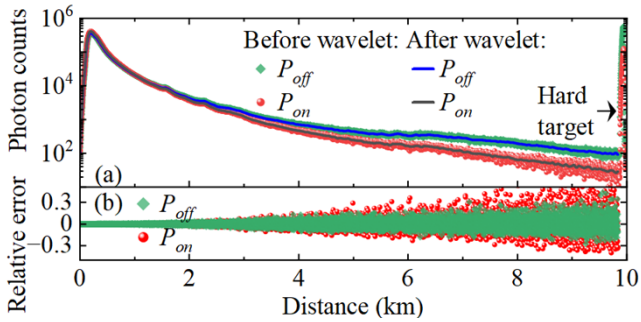

Fig. 3. (a) Comparison of the backscattered signals before and after wavelet filtering within 10 km at 1.5 m/5 min spatiotemporal resolution. (b) Relative errors between raw and filtered signals.

dead-time effects (missed counts within the detector recovery time) [9]. A typical backscattered profile is shown in Fig. 3(a), with a 5 min temporal resolution and a 1.5 m range resolution. The profiles extend to nearly 10 km, where a pronounced peak corresponds to the backscattered from a non-cooperative target. A peak within the first 1 km arises from the overlap function $Q(R)$, which approaches 100% at approximately 200 m. Owing to the extremely low system background and SNSPD dark counts, the detection operates at the quantum limit, where noise is dominated by photon shot noise following Poisson statistics. To reduce the fluctuations, wavelet denoising is applied. The MATLAB *wden* function was applied with a five-level *sym5* decomposition, the universal threshold ("sqtwolog") selection, soft thresholding, and the "sln" single-level noise threshold option. The denoised signals are plotted as solid lines in Fig. 3(a). As shown in Fig. 3(b), the mean difference between the pre- and post-filtering signals is close to zero, indicating that the filtering effectively preserves the original waveform while significantly improving the SNR.

Since x_{on} and x_{off} differ by only ~30 GHz, the parameters β, α_a, and α_m can be assumed wavelength-independent. Therefore, the ratio P_{on}/P_{off} can be written as:

$$P_{on}/P_{off} = \exp\left(-2\int_0^R [\alpha_{on} - \alpha_{off}]\, dr\right). \quad (3)$$

Then, the optical depth (OD) can be calculated as:

$$OD(R_j) = \int_0^{R_j} [\alpha_{on} - \alpha_{off}]\, dr = -0.5 \ln[P_{on}/P_{off}]. \quad (4)$$

Subsequently, the absorption difference caused by the gas, $\Delta\alpha$, can be written as:

$$\Delta\alpha(R_j) = \alpha_{\text{on}}(R_j) - \alpha_{\text{off}}(R_j) = OD(R_j)/R_j. \quad (5)$$

Then, $\Delta\alpha$ can further be expressed as the sum of the contributions from CO_2 and H_2O, as follows:

$$\Delta\alpha = N_{H_2O}(\sigma_{on-H_2O} - \sigma_{off-H_2O}) + N_{CO_2}(\sigma_{on-CO_2} - \sigma_{off-CO_2}), \quad (6)$$

where N_{CO_2} and N_{H_2O} are the molecular number densities of CO_2 and H_2O, respectively, and σ denotes the absorption cross section. To minimize the influence of water vapor and ensure accurate CO_2 retrieval, the laser wavelength is chosen at 1572.335 nm where H_2O absorption is negligible. By rearranging Eq. (6), the column-averaged CO_2 number density N_{CO_2} can be obtained as:

$$N_{CO_2} = \Delta\alpha/[(\sigma_{on-CO_2} - \sigma_{off-CO_2})]. \quad (7)$$

The CO_2 absorption cross section is obtained from the HITRAN database. Using the ideal gas law, N_{CO_2} can be converted to the column-averaged CO_2 concentration XI_{CO_2} as:

$$XI_{CO2} = N_{CO_2} \times 10^6/n = N_{CO_2} k_b T \times 10^6/P_r, \quad (8)$$

where n is the atmospheric molecular number density, P_r is the ambient pressure, T is the ambient temperature, and k_b is the Boltzmann constant, with P_r and T obtained from hourly averaged meteorological data provided by the local meteorological agency. To further reduce noise, a first-order Savitzky–Golay filter is applied to the retrieved XI_{CO_2} time-series profile. Based on Eq. (8), the X_{CO_2} within the range interval $[R_j, R_{j+1}]$ is given by:

$$X_{CO2}(R) = [XI(R_{j+1}) \cdot R_{j+1} - XI(R_j) \cdot R_j]/(R_{j+1} - R_j). \quad (9)$$

The advantage of the proposed algorithm lies in its use of XI_{CO_2}, which reflects the cumulative difference between P_{on} and P_{off} over the entire path from 0 to R. This difference is relatively large, resulting in a more robust retrieval. In contrast, the traditional method, illustrated in Fig. 3, begins with Eq. (5) by calculating the differential ΔOD, defined as:

$$\Delta OD(R_j) = OD(R_{j+1}) - OD(R_j). \quad (10)$$

Subsequently, the differential absorption coefficient over a unit range $dR = R_{j+1} - R_j$ is derived using Eq. (10), expressed as:

$$\Delta\alpha(R_{j+1} - R_j) = \Delta OD(R_j)/(R_{j+1} - R_j). \quad (11)$$

However, because $\Delta\alpha$ over a unit range dR is very small, the resulting P_{on}/P_{off} differential is minimal, making the retrieval highly noise-sensitive and requiring long averaging or coarse range bins for a stable X_{CO_2}.

To validate the system and algorithm, field experiments were conducted over three consecutive nights from 5 to 8 September 2025. The lidar was operated at night because the current receiver FOV of 0.78 mrad generates a strong daytime solar background. With a reduced FOV in future designs, continuous day-and-night operation will be achievable. The system was installed on the 5th floor of the Zhou Longquan Building at Xiamen University's Xiang'an campus and oriented toward the southeast coastal sector.

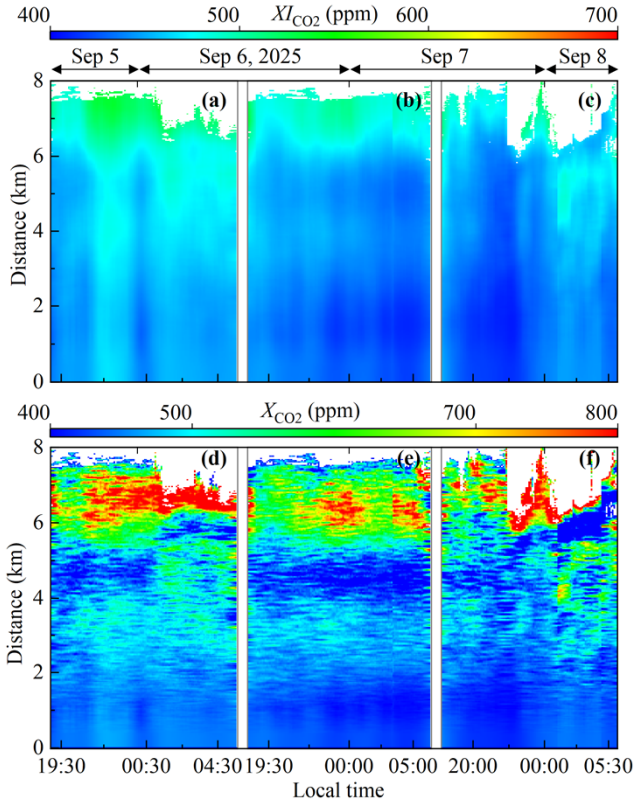

Fig. 4. Nighttime time–distance distributions of XI_{CO_2} (a)–(c) and range-resolved X_{CO_2} (d)–(f) from 5 to 8 September 2025, shown up to 8 km with 30 m/5 min resolution.

The range-resolved XI_{CO_2} and X_{CO_2} retrieved using the proposed algorithm at a 30 m range resolution are shown in Figs. 4(a) and 4(b), respectively. Data with an SNR below 7 were excluded. As seen in Fig. 4(a), the XI_{CO_2} retrieval exhibits a high SNR, which underpins the robustness of the X_{CO_2} profiles in Fig. 4(b). The results reveal persistent layering over the three nights of observations, with elevated X_{CO_2} occurring at approximately 2–4 km and 6–8 km. These enhancements are likely associated with nearby coastal industrial and high-traffic zones, and the stable nighttime boundary layer suppresses vertical mixing, allowing local emissions to accumulate. The elevated concentrations within these distance ranges also lead to a larger path-integrated XI_{CO_2} (10 km), as illustrated in Fig. 7.

In contrast, the traditional algorithm performs significantly worse. As shown in Fig. 5, it cannot recover a meaningful 30 m X_{CO_2} profile. Even at 300 m, the retrievals fluctuate strongly, and only at 600 m do they appear relatively smooth and broadly consistent with the proposed algorithm. Figure 6 further shows the 300 m retrieval from the traditional algorithm. Compared with Fig. 4(b), its X_{CO_2} fluctuations are substantially larger, and the difference from the new algorithm can reach nearly 100 ppm, highlighting the superiority of the proposed algorithm.

To verify the lidar-retrieved X_{CO_2}, concurrent *in-situ* CO_2 measurements were obtained outside the laboratory using a Picarro G2101-I analyzer. The comparison results are shown in Fig. 7. As seen, the first lidar measurement retrieved with the proposed algorithm agrees well with the *in-situ* observations, and their differences—summarized in the inset of

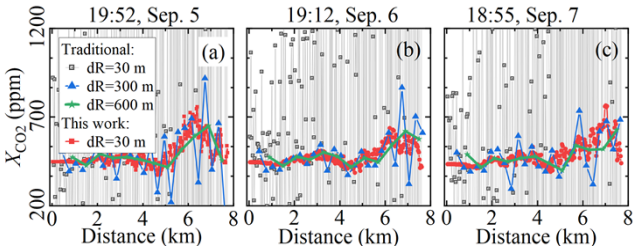

Fig. 5. X_{CO_2} profiles at three periods (a)–(c), comparing traditional retrievals ($dR = 30$, 300, 600 m) with the proposed 30 m retrieval.

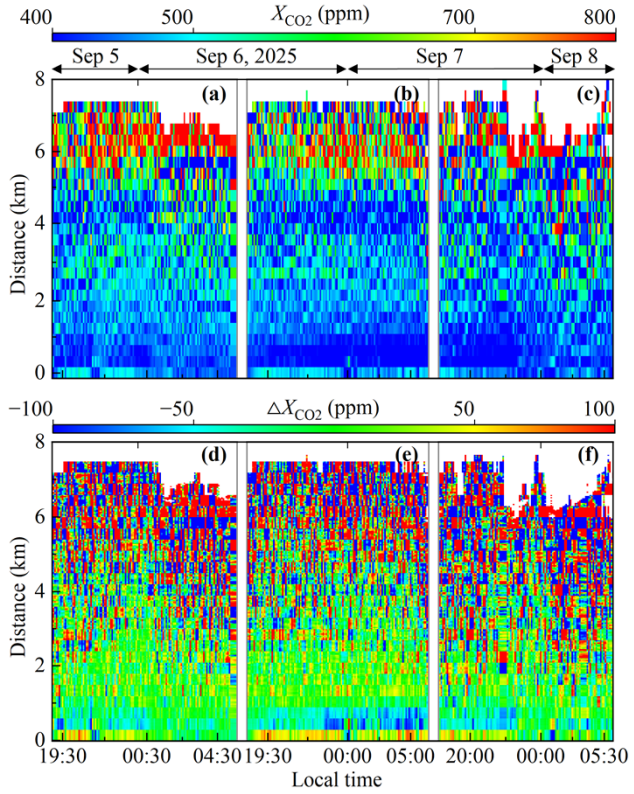

Fig. 6. (a)–(c) Same as Fig. 4 but showing X_{CO_2} retrieved with the traditional algorithm at $dR = 300$ m. (d)–(f) Differences (X_{CO_2}) between the traditional $dR = 300$ m retrieval and the proposed $dR = 30$ m retrieval.

Fig. 7(d)—yield a mean (μ) of −5.1 ppm and a standard deviation (σ) of 10.9 ppm. This bias is primarily attributed to local CO_2 emissions, as the laboratory is located near a roadway. For reference, the results derived from the traditional algorithm with a 300 m range resolution are also plotted in Fig. 7, with the corresponding difference statistics shown in Fig. 7(e). In this case, the μ and σ are 14.2 and 38.4 ppm, respectively. Despite using a range resolution that is ten times coarser, the traditional algorithm still exhibits a σ more than three times larger, further

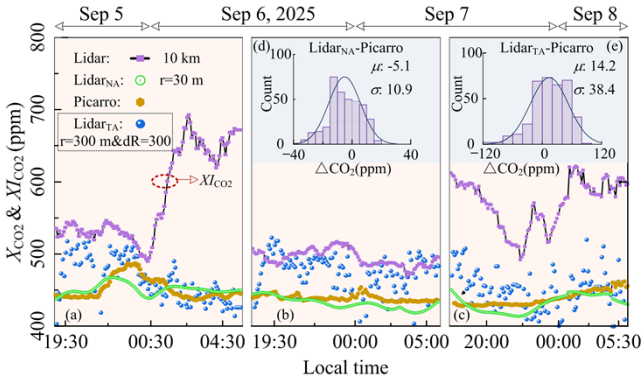

Fig. 7. (a)–(c) Comparison of the proposed X_{CO_2} ($dR = 30$ m) with Picarro over three nights, together with XI_{CO_2} (10 km) and traditional X_{CO_2} ($dR = 300$ m). (e) and (f) Statistical deviations from Picarro for the proposed and traditional X_{CO_2}. $Lidar_{NA}$ and $Lidar_{TA}$ denote the new- and traditional-algorithm retrievals, respectively.

demonstrating the improved robustness and reliability of the new algorithm.

In conclusion, this work establishes an effective pathway for resolving the long-standing tradeoff between detection range and retrieval resolution in CO_2 lidar. By combining photon-efficient detection with a stability-enhanced retrieval framework, the system delivers reliable fine-scale X_{CO_2} structures under real atmospheric conditions. The demonstrated capability provides a foundation for expanding high-resolution CO_2 observations and improving constraints in boundary-layer carbon-cycle studies.

Funding. Innovation Program for Quantum Science and Technology (2021ZD0303102); National Natural Science Foundation of China (42141001).

Disclosures. The authors declare no conflicts of interest.

Data availability. The data that support the findings of this study are available from the corresponding author upon reasonable request.

REFERENCES

1. M. E. Schlesinger and J. F. Mitchell, Rev. Geophys. **25**, 760 (1987).
2. J. V. G. de Arellano, B. Gioli, F. Miglietta, *et al.*, J. Geophys. Res.: Atmos. **109**, D18110 (2004).
3. J. B. Abshire, H. Riris, G. R. Allan, *et al.*, Tellus B: Chem. Phys. Meteorol. **62**, 770 (2010).
4. G. A. Wagner and D. F. Plusquellic, Opt. Express **26**, 19420 (2018).
5. G. Han, H. Zhang, Y. Huang, *et al.*, Remote Sens. Environ. **330**, 114954 (2025).
6. A. Amediek, A. Fix, G. Ehret, *et al.*, Atmos. Meas. Tech. **2**, 755 (2009).
7. J. Mao, J. B. Abshire, S. R. Kawa, *et al.*, Atmos. Meas. Tech. **17**, 1061 (2024).
8. E. Cadiou, D. Mammez, J.-B. Dherbecourt, *et al.*, Opt. Lett. **42**, 4044 (2017).
9. S. Yu, Z. Zhang, H. Xia, *et al.*, Light: Sci. Appl. **10**, 212 (2021).
10. S. Yu, K. Guo, S. Li, *et al.*, Opt. Express **32**, 21134 (2024).
11. W. Gong, A. Liang, G. Han, *et al.*, Photonics Res. **3**, 146 (2015).
12. M. Shangguan, H. Xia, C. Wang, *et al.*, Opt. Lett. **42**, 3541 (2017).